frontiers | Frontiers in Mechanical Engineering

TYPE Original Research
PUBLISHED 27 January 2026
DOI 10.3389/fmech.2025.1749899

OPEN ACCESS

EDITED BY
Yonggang Meng,
Tsinghua University, China

REVIEWED BY
Mladen Radojković,
University of Priština in Kosovska Mitrovica, Serbia
Yang Hu,
Shanghai University, China

*CORRESPONDENCE
Raphael Scharf,
raphael.scharf@unileoben.ac.at

RECEIVED 19 November 2025
REVISED 09 December 2025
ACCEPTED 10 December 2025
PUBLISHED 27 January 2026

CITATION
Scharf R, Pusterhofer M, Grün F and Staudinger P (2026) Simulation-based parameter optimization and experimental assessment of single- and multi-dimple textures in full-film lubrication.
Front. Mech. Eng. 11:1749899.
doi: 10.3389/fmech.2025.1749899

Simulation-based parameter optimization and experimental assessment of single- and multi-dimple textures in full-film lubrication

Raphael Scharf[1]*, Michael Pusterhofer[1], Florian Grün[1] and Paul Staudinger[2]

[1]Montanuniversität Leoben, Chair of Mechanical Engineering, Leobem, Austria, [2]Anton Paar, Graz, Austria

The specific geometrical modification of surfaces is a current field of research to enhance the tribological properties in lubricated sliding contacts. As many parameters influence the performance of textures, a numerical approach is used to identify optimal parameters for a single-dimple and multi-dimple textured convergent oil film gap. To ensure that such surface textures can be easily manufactured, the widely used milling manufacturing technique is employed. Additionally, a novel test methodology was implemented on a rheometer/tribometer to evaluate the performance of these textures in full-film lubrication. Both a numerical and an experimental approach are used. In this experimental methodology, the rotational speed, temperature, and minimum oil film gap are varied. The experiments show that the single-dimple texture leads to the highest load-carrying capacity. The drag force of both textures is similar at 23 °C and is lower than that of the untextured oil film gap. As the temperature increases, this beneficial effect of reducing drag is no longer observed. However, the load-carrying capacity of both textures remains higher than that of the untextured oil film gap.

KEYWORDS

convergent oil film gap, full-film lubrication, numerical and experimental approach, single- and multi-dimple textures, surface textures

1 Introduction

Bearings are widely employed in technical systems. The specific type selected depends on the machine and its operating requirements. For instance, rolling bearings are commonly used in compressors (Mikic et al., 2021). In power plants, hydrodynamic bearings are mostly used due to their long durability. According to Yang and Palazzolo (2021), in large power plants, approximately 1–2 MW are lost through friction by a single hydrodynamic thrust bearing. Consequently, many studies focus on different methodologies to reduce friction. For engine bearings, Ligier and Noel (2015) summarized the solutions to reduce friction into three categories:

- Material
- Geometry
- Environmental solutions

The modification of the lubricated sliding contact's geometry is becoming increasingly important. In 2025, 676 studies were found for the keyword "surface textures in tribology"

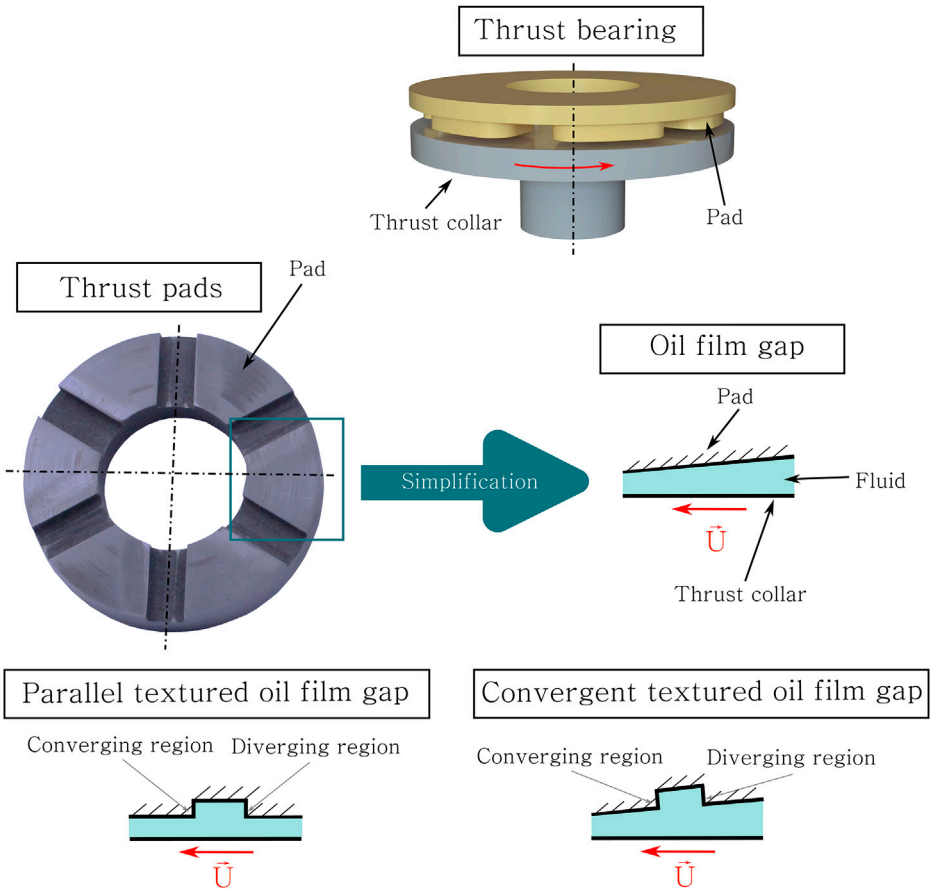

FIGURE 1
Schematic hydrodynamic thrust bearing.

on Sciencedirect.com, compared to 205 publications in 2015. However, Marian et al. (2022) mentioned that most studies focusing on the performance of textures in hydrodynamic lubrication use a parallel contact geometry. Because the oil film gap's geometry converges in many technical applications, this study will focus on a convergent oil film gap, as presented in Figure 1. The figure shows that the oil film gap of a hydrodynamic thrust bearing can be convergent, and a geometry simplification results in a convergent oil film gap. Furthermore, the figure shows that a texture consists of a converging and diverging region. For a parallel oil film gap, a dimple can significantly increase the load-carrying capacity compared to an untextured parallel oil film gap, where pressure build-up is not possible. In a textured convergent oil film gap, two converging regions overlap: the global convergent oil film gap and the textures' converging region.

The texture shape and its geometrical parameters considerably influences the performance, even in parallel contacts (Codrignani et al., 2020; Gherca et al., 2013; Guo et al., 2022; Kumar and Sharma, 2018; Shen et al., 2021; Singh and Awasthi, 2021; Uddin et al., 2017; Wei et al., 2020; Yu et al., 2010; Ren et al., 2007; Zhang et al., 2015; Pusterhofer et al., 2025; Wang Y. et al., 2025; Vencl et al., 2019). For instance, Wei et al. (2020) analyzed the performance of eight different multi-dimple textures on a convergent oil film gap and concluded that a square-shaped texture produces the highest dimensionless pressure. Codrignani et al. (2020) simulated seven different surface modifications, including single- and multi-dimple textures, for a sliding pin in full-film lubrication and reported that a single-dimple texture leads to the highest load-carrying capacity. This observation was confirmed by Fouflias et al. (2015), who numerically examined the performance of single- and multi-dimple textures on a parallel hydrodynamic thrust bearing.

In addition to the previously described relatively simple texture shapes, Su et al. (2024) investigated a bio-inspired texture numerically and found that this parabolic surface modification increases the load-carrying capacity. However, the manufacturing process of such bio-inspired textures is challenging.

Although according to Marian et al. (2022), approximately three-quarters of all publications in the field of surface texturing in tribology include an experimental approach, only a few publications use a test methodology for a convergent oil film gap. An external load is applied in the test methodology of Rosenkranz et al. (2019), Guo et al. (2018), and Pusterhofer et al. (2025), and the oil film gap height is measured. Pusterhofer et al. (2025) and Rosenkranz et al. (2019) evaluate the performance of different textures at different convergence ratios. According to Pusterhofer et al. (2025), textures reduce the hydrodynamic friction force but also the minimum oil film gap height over nearly all examined convergence ratios. Rosenkranz et al. (2019)

found that most textures are beneficial at high convergence ratios. Guo et al. (2018) focused on grooved textures and mentioned that for aspect ratios less than 1.5, there is no difference between the grooved and untextured experiments. Simply increasing the convergence ratio makes these surface modifications beneficial. Compared to these works, Henry et al. (2015), Wang W. et al. (2020), Wang J. et al. (2020), Morris et al. (2015), and Wang et al. (2001) present test methodologies for parallel oil film gaps. A special example of this methodology is the test rig used by Henry et al. (2015), who conducted experiments on square-shaped textures on a parallel thrust bearing for different texture area densities and different loads. They concluded that textures where a dimple is positioned at the inlet of an oil film gap considerably improve the tribological performance and that the thermal pad deformation creates convergent and divergent zones. Additionally, Henry et al. (2015) observed some cooling effects of textures of approximately 24 K.

This cooling effect was also observed by Wang W. et al. (2020), who used a ring-on-ring test rig to determine the impact of different grooved textures in mixed lubrication. They additionally mentioned that the friction coefficient COF decreases at different velocities (Wang W. et al., 2020).

Scharf et al. (2024a) numerically presented that small deviations from the optimal dimple geometry can deteriorate performance, highlighting the need for adequate manufacturing processes. Costa and Hutchings (2015) summarized these processes into four categories:

- Removing material
- Moving material
- Self-forming
- Adding material technologies

All manufacturing techniques have their specific advantages and disadvantages. Vencl et al. (2019) summarized the different surface methodologies presented in many articles and concluded that laser surface texturing is currently the most often used. According to Costa and Hutchings (2015), milling machines are a widely established material removal technique. Within this study, a texture that can be manufactured by such a machine should be found.

In Codrignani et al. (2020), Fouflias et al. (2015), and Codrignani et al. (2018), a single-dimple texture had the best performance. Therefore, this texture shape is selected and compared with a multi-dimple texture, both of which should be manufacturable with a milling machine.

A simulation algorithm is used to identify the optimal dimple parameters for specific conditions. Because experimental approaches for convergent oil film gaps are rare, a novel test methodology needed to be applied. In contrast to Pusterhofer et al. (2025) and Rosenkranz et al. (2019), the oil film gap height is applied to ensure full-film lubrication. The load-carrying capacity and friction can be measured.

As noted in the introduction, the effectiveness of textures is influenced by operating conditions, and most studies focus on parallel oil film gaps in full-film lubrication. This raises the question of how single- and multi-dimple textures perform under different conditions, such as rotational speed, minimum oil film gap height, and temperature.

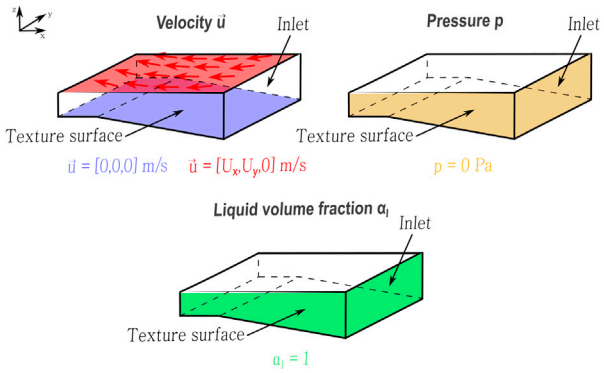

FIGURE 2
Boundary conditions for schematic oil film gap.

2 Methodology

2.1 Numerical approach

A simulation algorithm is required to identify the optimal texture geometry for specific conditions. A suitable simulation algorithm has already been published by Scharf et al. (2024a), Scharf et al. (2024b), and Scharf et al. (2025). Within this work, the performance of textures in full-film lubrication should be analyzed. Consequently, the multiphase Stokes flow, which considers cavitation and is presented through Equation 1, is used. In that equation, $\vec{u}$ represents the unknown velocity, and p is the unknown hydrodynamic pressure field. ρ stands for density, ν for kinematic viscosity, and ζ for the second viscosity of the fluid. $\boldsymbol{I}$ is the identity matrix, and $\vec{f}$ is the body force. The second viscosity ζ and ν are defined as the same value, which also confirms the inequality presented by Shibata et al. (2018). Additionally, the continuity equation (Equation 2) is necessary. If cavitation does not occur, solving the Stokes flow (cf. Equation 3) is sufficient.

$$-\nabla \cdot \left\{ \nu \left[\nabla \vec{u} + (\nabla \vec{u})^T - \frac{2}{3} (\nabla \cdot \vec{u}) I \right] + \zeta (\nabla \cdot \vec{u}) I \right\} + \nabla p = \rho \vec{f}, \quad (1)$$

$$\nabla \cdot \vec{u} = 0, \quad (2)$$

$$-\nu \Delta \vec{u} + \nabla p = \rho \vec{f}. \quad (3)$$

To consider cavitation, which occurs when the pressure p is less than the vapor pressure p_v, the Merkle algorithm (Merkle et al., 1998) is used, as presented in Equations 4–9. This cavitation model has been applied by Concli (2020) to simulate a hydrodynamic journal bearing and by Scharf et al. (2024a) and Scharf et al. (2024b) to simulate a convergent oil film gap. In this model, the vapor volume fraction α_v is calculated to determine the density ρ - and kinematic viscosity field ν, which are dependent on the density and viscosity of both the liquid ρ_l, ν_l and the vapor ρ_v, ν_v. The vapor volume fraction α_v represents the ratio of the vapor volume to the total volume $V_v + V_l$, where the sum of the liquid volume fraction α_l and vapor volume fraction α_v equals 1. The terms $\dot{m}^+$ and $\dot{m}^-$ describe the condensation and vaporization processes and are influenced by the condensation constant Cc, the evaporation constant Cv, the reference time t_∞, and velocity U_∞.

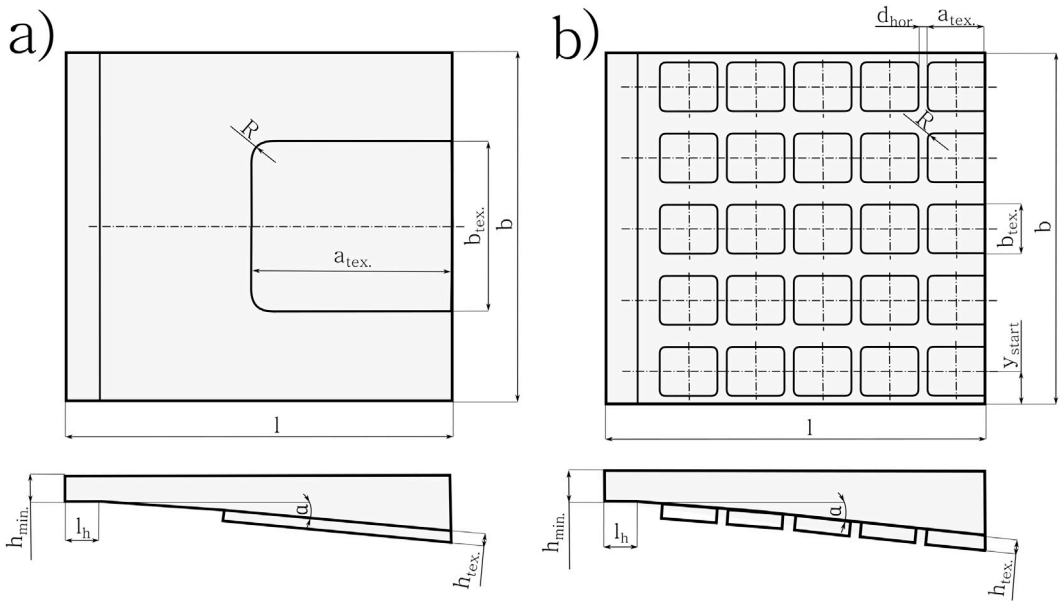

FIGURE 3
Geometrical parameters of oil film gap: **(a)** single-dimple texture and **(b)** multi-dimple texture.

$$\nabla \cdot (\vec{u}\,\alpha_v) = \dot{m}^+ - \dot{m}^-, \tag{4}$$

$$\dot{m}^+ = Cc\frac{\rho}{\rho_l \rho_v}\frac{(1-\alpha_l)}{0.5U_\infty^2 t_\infty} max\,(p - p_v, 0), \tag{5}$$

$$\dot{m}^- = Cv\frac{\rho}{{\rho_v}^2}\frac{\alpha_l}{0.5U_\infty^2 t_\infty} max\,(p_v - p, 0), \tag{6}$$

$$\alpha_v = \frac{V_v}{V_v + V_l}, \tag{7}$$

$$\rho = \rho_v\,\alpha_v + \rho_l\,(1-\alpha_v), \tag{8}$$

$$\nu = \nu_v\,\alpha_v + \nu_l\,(1-\alpha_v). \tag{9}$$

The schematic geometry of the oil film gap is depicted in Figures 2, 3. The finite element method (FEM) implemented in the Python package Netgen/NGSolve (NGSolve, 2025) is applied to solve the previously described partial differential equations. The Sparse Cholesky decomposition is used to solve the matrices. The geometry is discretized by tetrahedral-shaped elements with second-order shape functions. The maximal mesh size was determined through a grid study, resulting in a maximal mesh size of 100 µm being selected. Regarding the geometry of the oil film gap, Figures 2, 3 show a horizontal region on the left side. This surface is necessary to adjust the alignment of the pins (cf. Subsection 2.2) for the novel test methodology. This region is followed by a converging oil film gap. The boundary conditions for this numerical approach are depicted in Figure 2. The top surface is moving, the bottom surface is stationary, and ambient pressure is applied on the lateral surfaces. Consequently, the liquid volume α_l is equal to 1 on these surfaces. As a circular disc is used, the velocity field of the moving surface consists of horizontal and vertical components, as shown in Figure 2.

The simulation results include the pressure p and velocity $\vec{u}$ fields. To evaluate the performance of a specific oil film gap, the lifting force $\vec{F}_{lift}$ and drag force $\vec{F}_{drag}$ are computed (cf. Equations 10, 11). The lifting force $\vec{F}_{lift}$ is the integral of the hydrodynamic pressure p integrated over the top surface. The drag force is the integral of the shear stresses τ_x over the top surface.

$$\vec{F}_{lift.} = \int_A p_{(x,y,z=max)} \cdot \vec{n} dA, \tag{10}$$

$$\vec{F}_{drag.} = \int_A \tau_{x\,(x,y,z=max)} dA. \tag{11}$$

The required simulation parameters are presented in Table 1. HLP22 oil is used for lubrication, and the viscosity at 23 °C is calculated utilizing the Walther (1931) equation. The density ρ_l at different temperatures is estimated using the equation presented by GOST (2025). All other oil- and cavitation parameters are based on the work of Hong et al. (2018) and Savio et al. (2021).

Figure 3 illustrates the geometry of the single- and multi-dimple textures. To ensure manufacturability, the dimple geometry must be easily reproducible and cost-effective. Previous research has shown that rectangular textures are more effective than other simple dimple shapes (Scharf et al., 2025). Scharf et al. (2025) showed that textures that can cover a larger region, such as rectangular textures, perform better than other texture shapes (e.g., rectangular dimples). To ensure manufacturability, the edges are rounded with a radius R, which is defined by the minimum of $a_{tex.}/4$ and $b_{tex.}/4$.

An optimization algorithm is used to identify the optimal dimple parameters for specific conditions.

The negative performance enhancement ratio (PER), presented by Sharma et al. (2019) (cf. Equation 12), is used as the cost function for this optimization algorithm. Because such algorithms are designed to find a minimum, the negative PER value is defined as the cost function. This methodology was previously published by Scharf et al. (2025), and a Tree-structured Parzen Estimator (TPE) (Bergstra et al., 2025) is employed to determine the optimal parameters. A TPE is a variant of the Bayesian optimization algorithm (Watanabe, 2025), which categorizes parameters into

TABLE 1 Simulation parameters.

Parameter	
Density oil liquid ρ_l	854 kg/m^3
Density oil vapor ρ_v	0.13 kg/m^3
Dynamic viscosity liquid η_l	35.4 mPas
Dynamic viscosity vapor η_v	0.02 mPas
Condensation coefficient C_C	333
Vaporization coefficient C_v	0.00155
Vapor pressure p_v	165 Pa
Input velocity U_∞	2 m/s
Reference time t_∞	l/U_∞
Length of oil film gap l	12 mm
Horizontal length l_h	2 mm
Width of oil film gap b	10 mm
Minimum oil film thickness h_{min}	25 µm
Oil film gap angular α	0.16°
Convergence ration $h_{max}/h_{min} - 1$	1.12

TABLE 2 Interval of texture parameters.

Parameter	Single-dimple texture	Multi-dimple texture 5 × 5
Texture length $a_{tex.}$	[0.5, 0.6, … 9.9] mm	[0.5, 0.6, … 1.5] mm
Texture width $b_{tex.}$	[0.5, 0.6, … 9.9] mm	[0.5, 0.6, … 1.3] mm
Texture height $h_{tex.}$	[5, 10, … 30] µm	[5, 10, … 30] µm
Horizontal offset $d_{hor.}$	-	0.1 mm to $d_{hor.max}$
Vertical start position y_{start}	-	$b_{tex.}/2$ to $y_{start,max.}$

trials that perform better and those that do not (Wang L. et al., 2025). Initially, the parameters are defined randomly, and then the algorithm attempts to maximize the ratio between better-performing trials and the others (Wang L. et al., 2025). This process should guide parameter selection toward better-performing regions. The TPE sampler has the advantage of being able to be used for different data types (categorical, float, integer), which is essential for creating manufacturable textures.

$$PER = \frac{\frac{|\vec{F}_{lift,textured}|}{|\vec{F}_{lift,untextured}|}}{\frac{|\vec{F}_{drag,texured}|}{|\vec{F}_{drag,untextured}|}}. \quad (12)$$

In Table 2, the intervals for the optimization algorithm parameters are introduced. A categorized list of values for the possible optimal parameters is defined for the texture length $a_{tex.}$, width $b_{tex.}$, and height h_{tex}. The spacing interval for the multi-dimple texture depends on $a_{tex.}$ and $b_{tex.}$, causing the limits for $d_{hor.}$ and y_{start} to change, depending on $a_{tex.}$ and $b_{tex.}$. Therefore, a floating parameter interval is defined for $d_{hor.}$ and y_{start}. The limits

TABLE 3 Optimal dimple parameters.

Parameter	Single dimple texture	Multi-dimple texture 5 × 5
Texture length $a_{tex.}$	9.9 mm	1.5 mm
Texture width $b_{tex.}$	7.1 mm	1.3 mm
Texture height $h_{tex.}$	20 µm	20 µm
Horizontal offset $d_{hor.}$	-	0.1 mm
Vertical start position y_{start}	-	2.26 mm
PER	1.23	1.096

are set to ensure that the dimples do not overlap each other and do not protrude beyond the global oil film gap. Three parameters are varied for the single-dimple textures, and five parameters are varied for the multi-dimple texture.

The stopping criteria for both geometries were based on the number of trials. Specifically, 1000 simulations were conducted for the single-dimple texture, and 5000 simulations were conducted for the multi-dimple texture. Note that such a large number of simulations is not necessary to identify the optimal dimple parameters, as these were found within a few hundred numerical trials. However, the extensive dataset does allow for verification of whether the identified optimal parameters are indeed the best ones.

With the aid of the simulation algorithm described, the optimal dimple parameters were found and are depicted in Table 3. It is evident that the hyper-parameter toolbox aims to reduce the spacing between the dimples, as $d_{hor.}$ reaches the lower limit of the interval, and y_{start} reaches the upper limit of y_{start}. These results suggest that a single-dimple texture leads to a higher PER.

2.2 Experimental approach

Figure 4 depicts the test methodology using a modular compact rheometer MCR702e from Anton Paar. A specific oil film gap height $h_{min.}$ is adjusted to conduct the experiments. The generated normal force, which corresponds to the lifting force $\vec{F}_{lift}$ in the simulation approach, is measured. The basic principle of this experimental methodology is a three-pin-on-disc test rig. The disc rotates while the pins remain stationary. The pin specimen consists of three single pins arranged to avoid tilting effects and ensure that the MCR702e's air bearing is not loaded through shear forces. The resolution of the vertical displacement is approximately 0.6 µm, and the maximum tolerable normal load is 50 N. The load cell and sensor to measure the displacement are located in the upper part of the rheometer. The test cell itself is flooded with oil, and the splashback avoids oil contamination of the surrounding area. Additionally, this component serves as a type of oil storage, ensuring that the oil does not form a parabolic shape due to centrifugal force. In addition to the lifting force $\vec{F}_{lift}$, the drag moment $\vec{M}_{drag}$, the rotational speed n and the minimum oil film gap height h_{min} are measured.

The specimens must be accurately adjusted before each test. The axial runout of the disc and the vertical position of each pin are arranged. The axial runout is measured using a dial indicating gauge with a resolution of 2 µm. To quantify the vertical position of each

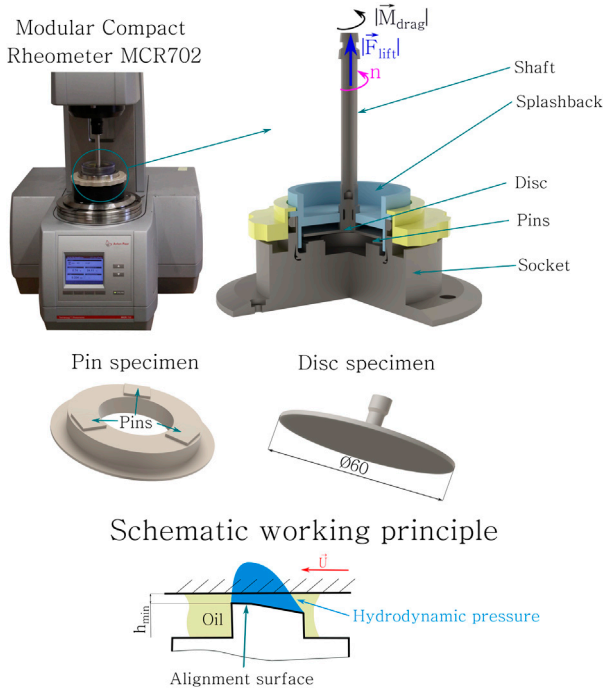

FIGURE 4
Test methodology.

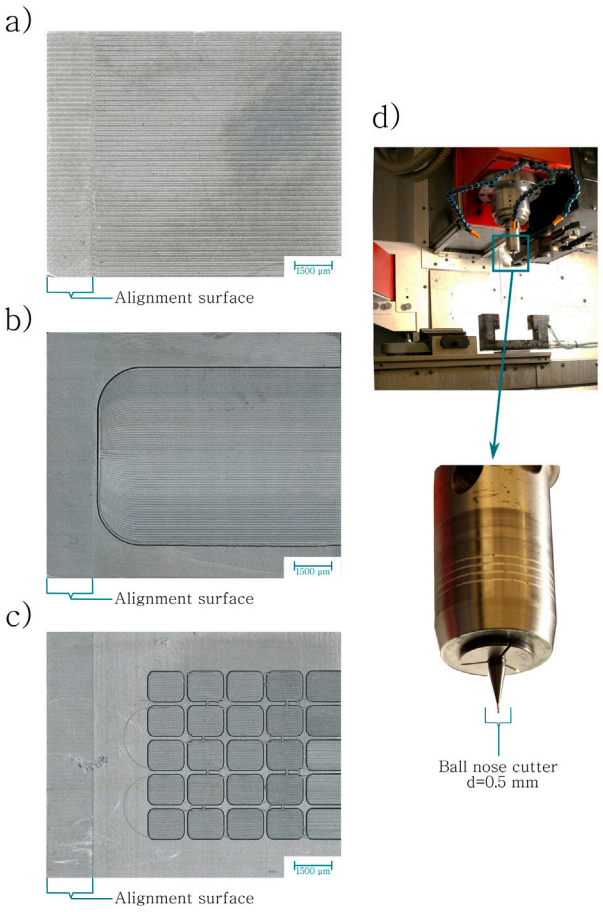

FIGURE 5
Pin surfaces and the manufacturing process: **(a)** untextured, **(b)** single-dimple texture, **(c)** multi-dimple texture, and **(d)** manufacturing technique.

pin, a feeler gauge stock is placed on the alignment surface of a pin, and a normal force of 1 N is applied to measure the vertical displacement for each pin. Feeler gauge stocks are added under the socket to adjust any displacement differences, achieving a height difference of less than 2 µm.

To determine the zero gap, a normal load of 1 N is applied when the oil bath is flooded and heated. This allows consideration of the thermal expansion.

As previously mentioned in this study, a three-axle milling machine is used to manufacture each texture presented in Table 3. A ball nose cutter (with a diameter of 0.5 mm) is installed in the milling machine (cf. Figure 5d). The manufacturing times for a complete specimen, consisting of three pins, are 4 h for a single-dimple and 6.5 h for a multi-dimple textured pin. It appears that the milling process is not as time efficient as estimated, but the milling machine used is not designed for high cutting speeds. The maximum spindle speed is limited to 8000 rpm, and the tool does not have an internal cooling system. Sommer et al. (2024), for example, used a high-speed milling machine with a maximum spindle speed of 45,000 rpm, which would significantly decrease the manufacturing time.

Figure 5 shows the surface of a single pin (untextured, single-dimple, and multi-dimple texture). The machining grooves are oriented in the direction of movement. The parallel alignment surface is located on the left side, followed by the converging region.

A contour measurement device, MarSurf VD140, is used to quantitatively evaluate the pin geometry. In Figure 6a, the methodology for evaluating the pin's surface is detailed. Using a tactile probe, the surface contour is measured over different horizontal lines with a displacement of 0.25 mm between each measurement. Figures 6b–d display the evaluated surface profiles. It can be observed that the surface is parallel up to 2 mm, followed by an inclination. Theoretically, the height difference for an angle of 0.16° and a length of 10 mm is 28 µm. This height difference is evident in Figure 6b–d. As the surface contour measurement device is used to evaluate the geometry of the texture, the y coordinates do not cover the entire area of 10 mm. Figures 6c–d show that the optimal texture parameters, for example, the textured depth $h_{tex.}$ of 20 µm, can be achieved with this common manufacturing technique. The irregularities in the height profile at different y coordinates can be attributed to the different tool tracks.

These different tool tracks also influence the roughness of the pins, as presented in Table 4. For the untextured specimens, the surface roughness is measured three times for each pin, perpendicular to the lay direction. The roughness parameters for the single-dimple texture are determined inside the dimple (two tracks per pin) and outside the dimple (one track per pin). Due to the limited space inside the dimples for the multi-dimple textures, the roughness parameters are measured outside the dimples, twice for each pin. The disc roughness is analyzed in the radial direction four times.

Standard aluminum discs are used for the disc material in the pin-on-disc test rig. The pins are made from stainless steel, and hydraulic oil HLP22 (LIQUI MOLY GmbH, 2025) is used as the lubricant (cf. Table 5).

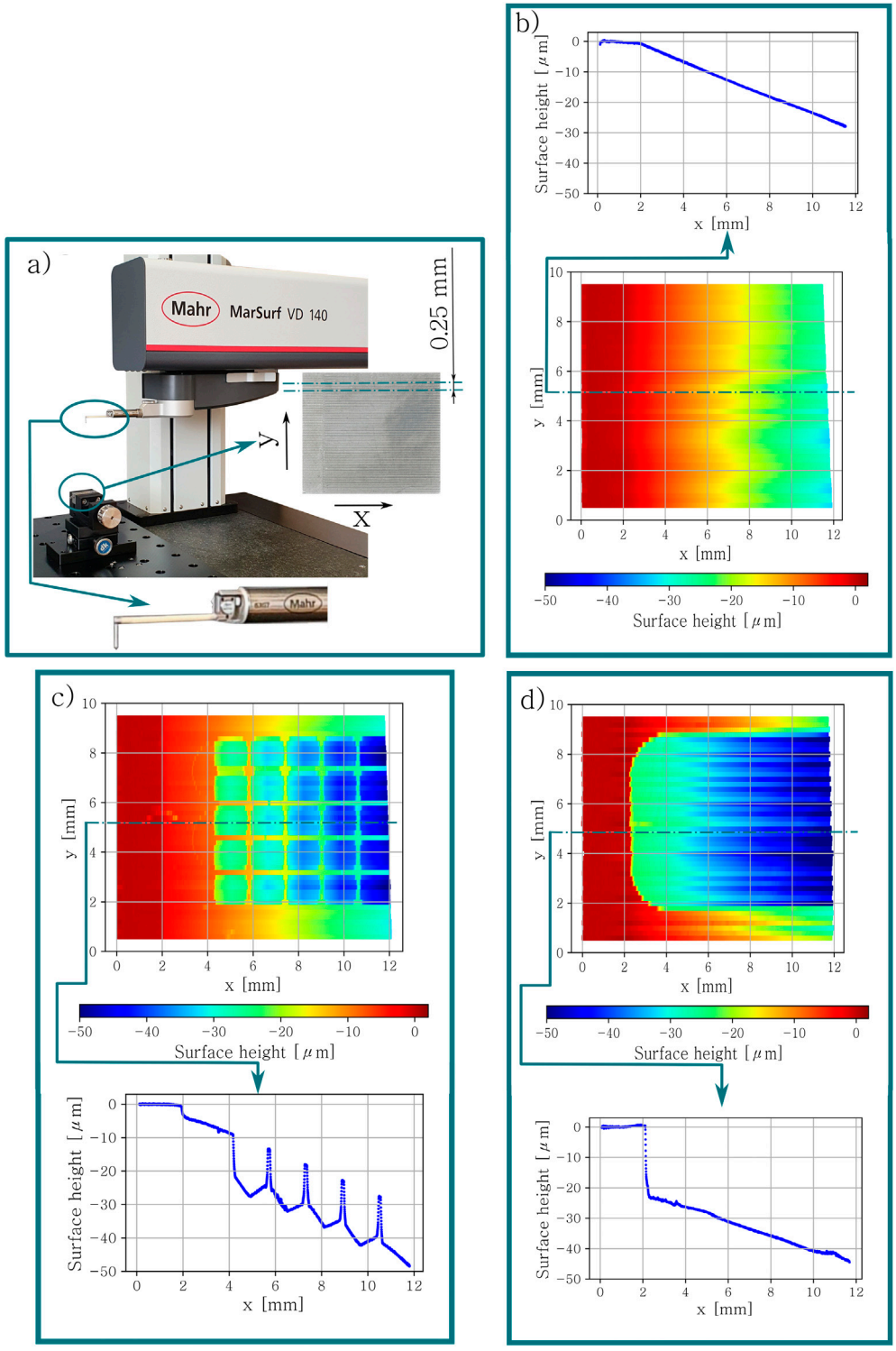

FIGURE 6
Evaluation of pin surface: **(a)** methodology, **(b)** untextured pin, **(c)** multi-dimple textured pin, and **(d)** single-dimple textured pin.

2.3 Test strategy

Each experiment consists of three different stages (cf. Figure 7):

- Heating
- Adjustment of oil film gap height $h_{min.}$
- Testing

During the heating period, the oil film gap height $h_{min.}$ is set at 1 mm, and the disc rotates at 300 rpm to establish a uniform temperature field. This is followed by the adjustment of the oil film gap height, where the minimum film thickness $h_{min.}$ is defined.

TABLE 4 Surface roughness.

	Untextured specimen		Disc	
	Ra [µm]	Rz [µm]	Ra [µm]	Rz [µm]
Average	0.227	0.943	0.5735	2.789
Min	0.148	0.954	0.565	2.296
Max	0.340	1.576	0.589	2.989
	Single-dimple texture		Multi-dimple texture	
	Inside dimple		Inside dimple	
Average	0.459	2.126	Not measurable	
Min	0.326	1.978		
Max	0.619	2.559		
	Outside dimple		Outside dimple	
Average	0.163	1.015	0.114	0.771
Min	0.133	0.905	0.089	0.6525
Max	0.19	1.184	0.129	0.952

TABLE 5 Specimen materials.

Material	
Disc	6082 Aluminum (3.2315)
Pin	Stainless steel (1.4301)
Oil	HLP22

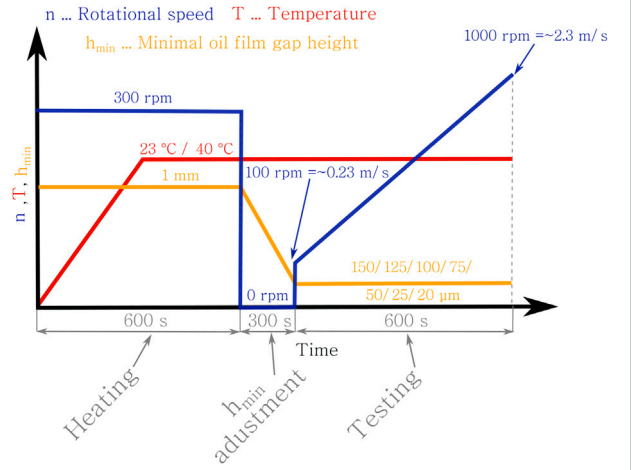

FIGURE 7
Test strategy.

During this process, the disc is stationary. The final stage is the testing phase, where the rotational speed is increased from 100 rpm to 1000 rpm, which corresponds to a magnitude of the velocity between 0.23 m/s and 2.3 m/s. Two different temperature levels (23 °C and 40 °C) were tested, along with seven different minimum oil film gap heights $h_{min.}$. The minimum oil film gap height $h_{min.}$ is controlled and measured during the experiment to prevent the bodies from coming into contact. To evaluate churning losses, a test with a minimum oil film gap height $h_{min.}$ of 1 mm is conducted. The drag moment $\vec{M}_{drag}$ is subtracted from the results obtained to identify the friction in the tribological contact.

3 Results

3.1 Experimental results

Figure 8 shows specific test graphs for different pin geometries. Generally, it can be observed that with increasing rotational velocity, the lifting force $\vec{F}_{lift}$ and drag force $\vec{F}_{drag}$ increase. Furthermore, the temperature measured at the bottom of the oil bath is constant at 40 °C during the testing period. Although the control system to keep the minimum oil film gap height constant was enabled, these graphs illustrate that the minimum oil film gap height $h_{min.}$ increases with increasing rotational speed. Theoretically, a minimum oil film gap height $h_{min.}$ = 25 µm is defined in the graphs of Figure 8. This defined value is only maintained at the beginning of the experiment. With increasing normal load, $h_{min.}$ also increases stepwise. Further experiments have shown that this behavior is more dominant at lower minimum oil film gap heights $h_{min.}$ (cf. excerpt of the experimental results in the appendix). Therefore, the increasing lifting force $\vec{F}_{lift}$ with decreasing $h_{min.}$ could potentially explain this phenomenon. Note that $h_{min.}$ is measured as a displacement of the air bearing.

Regarding the performance of different texture geometries, the single-dimple texture leads to the highest lifting force $\vec{F}_{lift}$, followed by the multi-dimple texture and the untextured oil film gap (cf. Figure 8). This trend was also seen at a temperature of 23 °C and with other minimum oil film gap heights $h_{min.}$

Referring to the drag force $\vec{F}_{drag}$, Figure 8 shows that the $\vec{F}_{drag}$ of both textures is quite similar, and it is greater than the $\vec{F}_{drag}$ of the untextured oil film gap. Additional experiments revealed a controversial result at 23 °C. At this temperature level, the $\vec{F}_{drag}$ of both textures is also similar, but less than the $\vec{F}_{drag}$ of the untextured pin (cf. Figure 9). However, note that the drag force $\vec{F}_{drag}$ is, in general, low, up to approximately 0.3 N at room temperature, depending on the rotational speed n, the oil film gap height $h_{min.}$, and the surface of the pin.

3.2 Comparison with the simulation model

Figure 9 presents the experimental and numerical results for specific conditions. Similar to Figure 8, $h_{min.}$ increases with increasing $\vec{F}_{lift}$. For the simulated points, the effective $h_{min.}$ is determined according to the experimental results. Consequently, there appear to be some fluctuations in the numerical results, which are a result of varying two parameters: rotational speed n and minimum oil film gap height $h_{min.}$. The trends and rankings between the numerical and experimental results are similar, but there is an offset between them. This difference could be explained by a higher temperature in the oil film gap, which reduces the

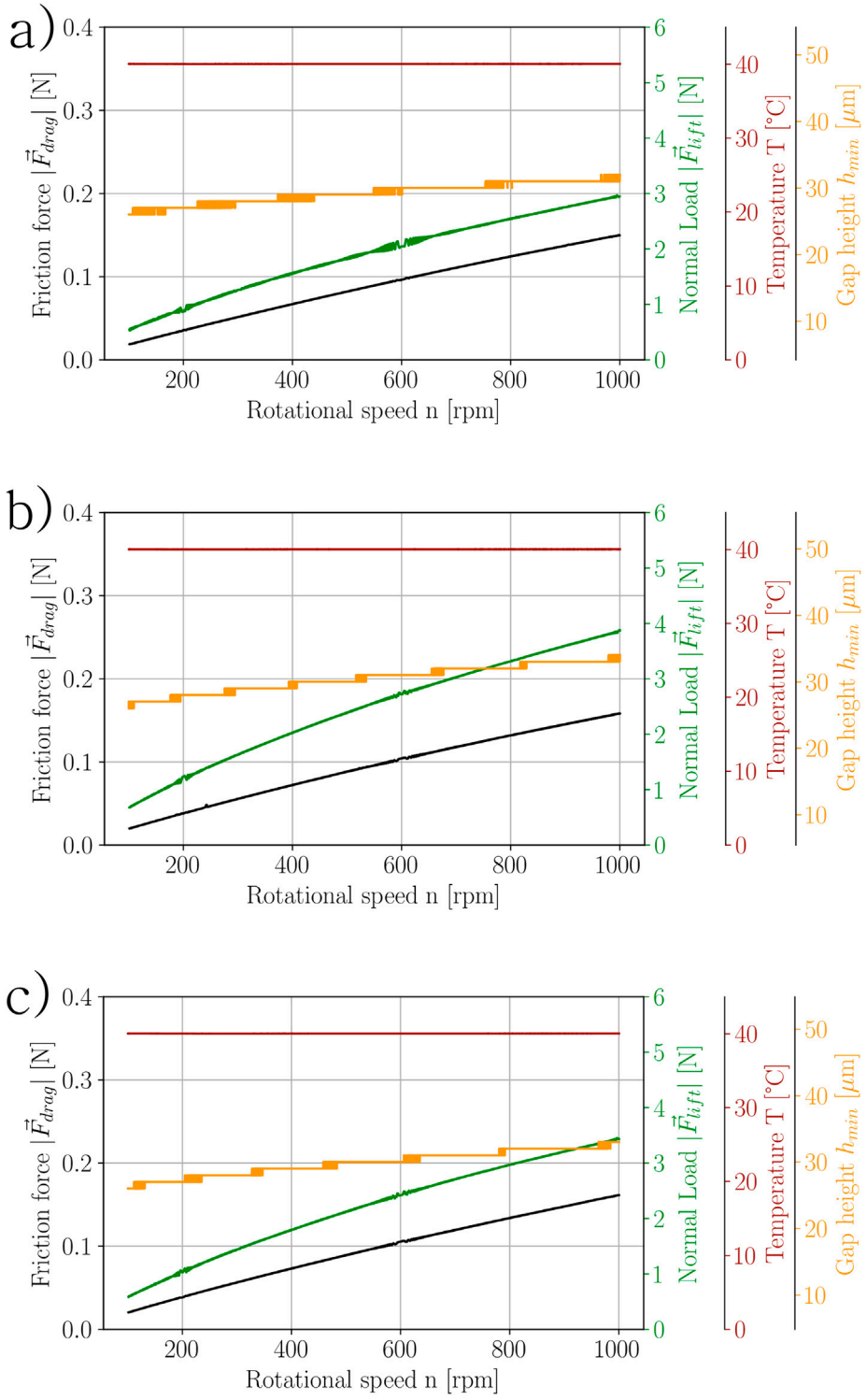

FIGURE 8
Test graph for **(a)** untextured, **(b)** single-dimple textured, and **(c)** multi-dimple textured oil film gaps.

viscosity, or through the observation that, according to DIN 51524-2 (2017), the kinematic viscosity of an HLP22 can vary between 19.8 mm^2/s and 24.2 mm^2/s, or a combination of both factors. Henry et al. (2015) found that the temperature inside the oil film gap is significantly higher. They measured the temperature at various positions in a hydrodynamic thrust bearing and concluded that the temperature can increase by approximately 10 K (Henry et al., 2015). As the temperature increases, the oil viscosity decreases, resulting in a decrease in the lifting force $\vec{F}_{lift}$. This effect is especially significant at low temperatures. At a temperature of 23 ˚C, a temperature

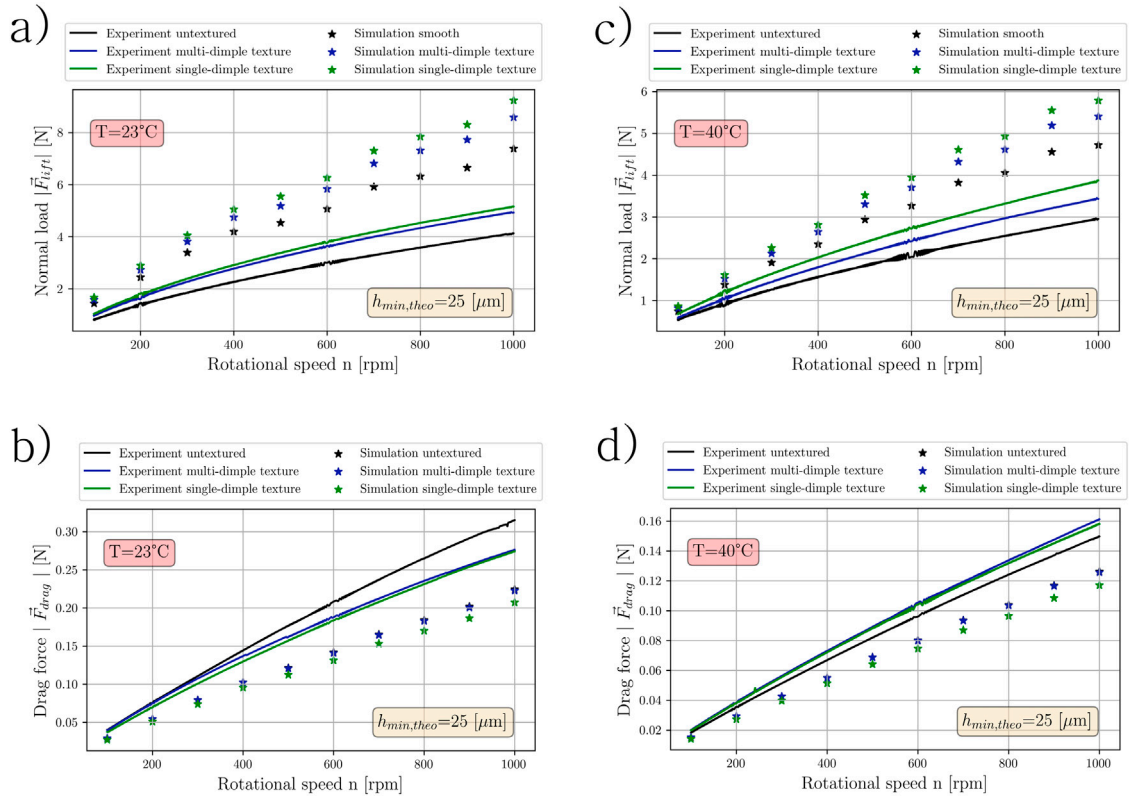

FIGURE 9
Comparison between simulation and experimental results. **(a)** F_{lift} over n at T = 23 °C, h_{min} = 25 µm, **(b)** F_{drag} over n at T = 23 °C, h_{min} = 25 µm, **(c)** F_{lift} over n at T = 40 °C, h_{min} = 25 µm, and **(d)** F_{drag} over n at T = 40 °C, h_{min} = 25 µm.

increase of 10 K leads to a 40% decrease in viscosity for the oil used in this study. Consequently, the numerical results overestimate the lifting force $\vec{F}_{lift}$. It can be observed that the relative difference between the numerical and experimental results decreases as the temperature increases. This also supports the potential mechanism, as at higher temperatures, there are fewer viscosity deviations due to temperature deviations. Regarding the drag force $\vec{F}_{drag}$, it should be noted that these values are generally low, making them difficult to evaluate. Although the churning losses are determined at a minimum oil film gap height $h_{min.}$ of 1 mm, it is possible that the churning losses vary, leading to overestimation of the drag force in the experiments. The difficulty of achieving the same numerical and experimental results was also mentioned by Wang et al. (2021), where a laser-textured surface pin-on-disc contact is analyzed. They compared the simulated and measured coefficient of friction COF and found a significant deviation between the values (Wang et al., 2021). Nevertheless, this test methodology can be used to identify similar trends as the simulation would predict.

4 Discussion

4.1 Discussion of dimple parameters

The simulation algorithm showed that a single-dimple texture leads to a higher PER than the multi-dimple texture (cf. Table 3). This observation was also mentioned by Codrignani et al. (2020), although they simulated a pin-on-disc contact with a minimum oil film gap height $h_{min.}$ of 1 µm and a velocity of 0.1 m/s. In this work, a significantly higher oil film gap and greater velocity were analyzed. This single-dimple texture resembles a Rayleigh step, which is already known in the literature. Rahmani et al. (2009) found that the optimal length of such a step is 70% of the oil film gap length for a parallel slider. In this study, the length of the texture $a_{tex.}$ is 83% of the slider's length l, but it should be noted that this is the upper limit of the examined interval, which was defined to guarantee a manufacturable texture geometry. Additionally, note that in this study, the performance of a convergent oil film gap is analyzed, which means that two converging regions overlap, as presented in Figure 1. Regarding the texture width $b_{tex.}$ Bei et al. (Rahmani et al., 2009) concluded that for rectangular textures on a convergent oil film gap, the optimal width $b_{tex.}$ is approximately 70% of the oil film gap width b. This observation can also be found in Table 3, where the optimal texture width $b_{tex.}$ is 71% of the complete width b.

Liu et al. (2019) investigated the performance of micro dimples for a parallel oil film gap and found that the optimal texture height $h_{tex.}$ is 30 µm to increase the pressure the most for a minimum oil film gap height $h_{min.}$ of 30 µm. In this study, the optimal texture height $h_{tex.}$ is 20 µm for a minimum oil film gap height $h_{min.}$ equivalent to 25 µm. Although Liu et al. (2019) simulated a parallel

oil film gap, their work and this study present similar optimal texture heights $h_{tex.}$.

As already mentioned, the optimization algorithm tries to reduce the spacing by searching for parameters that reduce the spacing between the dimples. Xing et al. (2021) focused on the performance of multi-dimple textures on a parallel oil film and showed that with increasing spacing perpendicular to the movement direction, the load-carrying capacity decreases. This phenomenon matches the results obtained in this work. Xing et al. (2021) explored the influence of the spacing in the movement direction and showed that with increasing spacing in the movement direction, the load-carrying capacity decreases starting with a spacing length of 10 µm. Below this 10 µm, the load-carrying capacity increases (Xing et al., 2021). It should be noted that Xing et al. (2021) changed the global geometry of the oil film gap depending on the spacing distance and evaluated the average fluid pressure. So, in the case of increasing spacing at constant dimple geometries, the average hydrodynamic pressure is lower than that of smaller spacing because the relative area of the converging region, related to the area of the oil film gap, becomes lower. Nevertheless, similar trends in this work and in Xing et al. (2021) could be observed because the minimum spacing was defined as 100 µm.

4.2 Discussion of the test methodology

As mentioned in the introduction, most publications use a test methodology for parallel oil film gaps. Pusterhofer et al. (2025), Rosenkranz et al. (2019), and Guo et al. (2018) used a test rig to evaluate the performance of textures in full-film lubrication by applying an external force and measuring the minimum oil film gap height $h_{min.}$. This differs from the methodology of this article, where the oil film gap height $h_{min.}$ is applied, and the resulting lifting force $\vec{F}_{lift}$ is measured. This principle can prevent mixed lubrication, but Figure 8 shows that $h_{min.}$ is not kept constant with increasing lifting force $\vec{F}_{lift}$, as previously mentioned.

Guo et al. (2018) conducted their experiments at low velocities, less than 0.02 m/s, compared to Rosenkranz et al. (2019) (1 m/s) and Pusterhofer et al. (2025) (5 m/s). The test methodology used in this work varies the velocity between 0.23 m/s and 2.3 m/s. Additionally, glass discs are required for the methodology described by Rosenkranz et al. (2019) and Guo et al. (2018) to measure the oil film thickness with optical devices. Pusterhofer et al. (2025) developed a test methodology using an eddy current sensor to measure the minimum oil film gap height $h_{min.}$ This sensor specification is also calibrated for a specific disc material. The test methodology presented in this study has the advantage of measuring the minimum oil film gap height $h_{min.}$ in the air bearing, eliminating the influence of specimen material on the measurement, in contrast to Pusterhofer et al. (2025), Rosenkranz et al. (2019), and Guo et al. (2018).

Because the viscosity of the oil is temperature dependent, the control of temperature is crucial. Rosenkranz et al. (2019) and Pusterhofer et al. (2025) published that the oil is pumped to the contact. In Rosenkranz et al. (2019), the oil temperature at the inlet ranges from 23.5 °C to 26 °C, while Pusterhofer et al. (2025) did not control the oil temperature. No information regarding temperature is provided Guo et al. (2018). This study uses a fully flooded oil bath, allowing precise temperature adjustment. Nevertheless, it should be noted in the tribological contact itself that the temperature potential is higher. For instance, Henry et al. (2015) measured a temperature difference of over 10 K in the tribological contact.

Friction force measurement is complex due to the small values. Rosenkranz et al. (2019) determined the friction force by small displacements of the load arm, while Pusterhofer et al. (2025) measured the friction force by an integrated mounted force cell. Guo et al. (2018) do not consider drag force. In the test methodology of the module compact rheometer MCR702e, the friction moment is measured by the current in the engine. The installed air bearing reduces friction losses significantly. Therefore, this solution does not depend on any displacements.

Although the presented test methodology has specific advantages, the manufacturing process of the pin specimens is complex, as the convergent region must be manufactured and cannot be adjusted, unlike Pusterhofer et al. (2025), Rosenkranz et al. (2019), and Guo et al. (2018).

In terms of the lubrication system, this test methodology has an advantage, as the oil bath is fully flooded. This allows for easy consideration of thermal expansion when heating the complete specimens. In Pusterhofer et al. (2025), Rosenkranz et al. (2019), and Guo et al. (2018), the oil is transported through a pipe and supplied to the contact, which may pose challenges when conducting experiments at higher temperatures, if hot oil is only added to the surface.

4.3 Discussion of the test results

Codrignani et al. (2020) and Fouflias et al. (2015) show numerically that single-dimple textures can increase the lifting $\vec{F}_{lift}$ and drag force $\vec{F}_{drag}$ more than multi-dimple textures. This behavior is observed in this study (cf. Figures 8, 9). Theoretically, $h_{min.}$ should be kept constant, but with an increasing lifting force $\vec{F}_{lift}$, $h_{min.}$ increases. As $h_{min.}$ of both textures increases more than the untextured oil film gap, this could be an indicator of the beneficial behavior of surface textures, as presented in Figure 8.

Zhang et al. (2015), Fouflias et al. (2015), Babu et al. (2021), and Ullah et al. (2021) investigated the performance of different dimple geometries in different velocity intervals numerically. They show that the ranking of the performance, including lifting $\vec{F}_{lift}$ and drag force $\vec{F}_{drag}$, over their analyzed velocity interval does not change. This behavior also is observed in this study and is depicted in Figures 8, 9.

The influence of different temperatures, corresponding to different viscosities, is examined by Gao and Chen (2020). They conducted experiments on parallel grooved textured oil film gaps. They found that the reduction of the load-carrying capacity with increasing temperature is not constant for all analyzed grooves (Gao and Chen, 2020). Because their reference is a parallel oil film gap, the comparison between this study and their work is not useful, because their reference experiments result in a lifting force $\vec{F}_{lift}$ of approximately 0 N. However, Figure 9 shows that with increasing temperature, the beneficial effect of textures, which decreases the drag force $\vec{F}_{drag}$ compared to an untextured oil film gap, can no longer be observed. Nevertheless, the surface modifications increase

the lifting force, compared to the untextured oil film, even at higher temperatures.

5 Conclusion

Within this study, a numerical algorithm similar to those used by Radojkovic et al. (2023) and Joksic et al. (2023) is used to identify the optimal dimple parameters. A novel test methodology is established, and the performance of single-dimple, multi-dimple, and untextured pins is experimentally and numerically compared.

In summary, it can be concluded:

- The optimal dimple parameters for a single-dimple and multi-dimple texture were found numerically with focus on textures that can be manufactured through a prevalent milling manufacturing technique.
- Although the manufacturing process for dimples with a depth of 20 µm is challenging, it has been shown that it is possible to produce these textures.
- A novel test methodology on a module compact rheometer MCR702e was developed.
- Experiments with untextured, single-dimple, and multi-dimple textured pins were conducted under varying conditions (rotational speed n, minimum oil film gap height $h_{min.}$, and temperature, T).
- The results illustrate that the single-dimple texture leads to the highest lifting force $\vec{F}_{lift}$, compared to the multi-dimple texture and the untextured pin.
- With increasing temperature T, the beneficial effect of textures decreasing the drag force $\vec{F}_{drag}$, compared to the untextured oil film gap, can no longer be observed. However, the lifting force $\vec{F}_{lift}$ of both textures is higher, relative to the untextured oil film gap.

More experiments and simulations are required to develop a deeper understanding of the performance of textures under varying conditions. It would be interesting to investigate the performance of different convergent oil film gap angles α and the influence of specimen alignment. Consequently, the performance of surface modifications could be analyzed for specifically defined axial run-outs. Additionally, studying the performance of these textures under mixed lubrication would be valuable. However, due to the normal load limitations of the test rig, another test methodology must be developed.

Data availability statement

The original contributions presented in the study are included in the article/Supplementary Material; further inquiries can be directed to the corresponding author.

Author contributions

RS: Conceptualization, Data curation, Formal analysis, Investigation, Methodology, Project administration, Software, Validation, Visualization, Writing – original draft. MP: Conceptualization, Project administration, Supervision, Writing – review and editing. FG: Project administration, Supervision, Writing – review and editing. PS: Conceptualization, Methodology, Writing – review and editing.

Funding

The author(s) declared that financial support was not received for this work and/or its publication.

Conflict of interest

Author PS was employed by Anton Paar.

The remaining author(s) declared that this work was conducted in the absence of any commercial or financial relationships that could be construed as a potential conflict of interest.

Generative AI statement

The author(s) declared that generative AI was not used in the creation of this manuscript.

Any alternative text (alt text) provided alongside figures in this article has been generated by Frontiers with the support of artificial intelligence and reasonable efforts have been made to ensure accuracy, including review by the authors wherever possible. If you identify any issues, please contact us.

Publisher's note

Supplementary Material

The Supplementary Material for this article can be found online at: https://www.frontiersin.org/articles/10.3389/fmech.2025.1749899/full#supplementary-material

References

Babu, P. V., Ismail, S., and Ben, B. S. (2021). Experimental and numerical studies of positive texture effect on friction reduction of sliding contact under mixed lubrication. *Proc. Institution Mech. Eng. Part J J. Eng. Tribol.* 235 (2), 360–375. doi:10.1177/1350650120930911

Bergstra, J. S., Bardenet, R., Bengio, Y., and Kégl, B. (2025). Algorithms for hyper-parameter optimization.

Codrignani, A., Frohnapfel, B., Magagnato, F., Schreiber, P., Schneider, J., and Gumbsch, P. (2018). Numerical and experimental investigation of texture shape and

position in the macroscopic contact. *Tribol. Int.* 122, 46–57. doi:10.1016/j.triboint.2018.02.001

Codrignani, A., Savio, D., Pastewka, L., Frohnapfel, B., and van Ostayen, R. (2020). Optimization of surface textures in hydrodynamic lubrication through the adjoint method. *Tribol. Int.* 148, 106352. doi:10.1016/j.triboint.2020.106352

Concli, F. (2020). "Equilibrium of a journal bearing: a simplified CFD-analytical coupled approach," in *Advances in fluid mechanics XIII* (PressSouthampton UK: WIT), 13–25. doi:10.2495/AFM200021

Costa, H. L., and Hutchings, Im (2015). Some innovative surface texturing techniques for tribological purposes. *Proc. Institution Mech. Eng. Part J J. Eng. Tribol.* 229 (4), 429–448. doi:10.1177/1350650114539936

DIN 51524-2 (2017). Druckflüssigkeiten - Hydrauliköle - Teil 2: Hydrauliköle HLP, mindestanforderungen.

Fouflias, D. G., Charitopoulos, A. G., Papadopoulos, C. I., Kaiktsis, L., and Fillon, M. (2015). Performance comparison between textured, pocket, and tapered-land sector-pad thrust bearings using computational fluid dynamics thermohydrodynamic analysis. *Proc. Institution Mech. Eng. Part J J. Eng. Tribol.* 229 (4), 376–397. doi:10.1177/1350650114550346

Gao, H., and Chen, X. (2020). Effect of surface texturing on hydrodynamic lubrication at various temperatures. *AIP Adv.* 10 (5), 055301. doi:10.1063/1.5143686

Gherca, A. R., Maspeyrot, P., Hajjam, M., and Fatu, A. (2013). Influence of texture geometry on the hydrodynamic performances of parallel bearings. *Tribol. Trans.* 56 (3), 321–332. doi:10.1080/10402004.2012.752550

GOST (2025). State system for ensuring the uniformity of measurements for the density of oil. The tables for recalculation, R 8.610–2004.

Guo, L., Wong, P., and Gachot, C. (2018). Facilitating the study of the texturing effect on hydrodynamic lubrication. *Lubricants* 6 (1), 18. doi:10.3390/lubricants6010018

Guo, Q., Zheng, L., Zhong, Y., Wang, S., and Ren, L. (2022). Numerical simulation of hydrodynamic lubrication performance for continuous groove-textured surface. *Tribol. Int.* 167, 107411. doi:10.1016/j.triboint.2021.107411

Henry, Y., Bouyer, J., and Fillon, M. (2015). An experimental analysis of the hydrodynamic contribution of textured thrust bearings during steady-state operation: a comparison with the untextured parallel surface configuration. *Proc. Institution Mech. Eng. Part J J. Eng. Tribol.* 229 (4), 362–375. doi:10.1177/1350650114537484

Hong, B., Lv, S., Liu, Q., Jour, J., Ji, Y., Gao, Z., et al. (2018). A simple method to evaluate the vapor pressure of transformer oil at various temperatures. *Adv. Eng. Res.* 2018 (170).

Joksic, S., Radojkovic, M., Sarkocevic, Z., Milojevic, S., and Stojanovic, B. (2023). *Deformation analysis of gear shift fork with mass optimization, 14th DQM international conference Life Cycle Engineering and Management DQM-POLYTECH-2023*. Serbia: Prijevor.

Kumar, V., and Sharma, S. C. (2018). Influence of dimple geometry and micro-roughness orientation on performance of textured hybrid thrust pad bearing. *Meccanica* 53 (14), 3579–3606. doi:10.1007/s11012-018-0897-0

Ligier, J.-L., and Noel, B. (2015). Friction reduction and reliability for engines bearings. *Lubricants* 3 (3), 569–596. doi:10.3390/lubricants3030569

LIQUI MOLY GmbH (2025). Produktinformationen hydrauliköl HLP 22.

Liu, W., Ni, H., Chen, H., and Wang, P. (2019). Numerical simulation and experimental investigation on tribological performance of micro-dimples textured surface under hydrodynamic lubrication. *Int. J. Mech. Sci.* 163 (6), 105095. doi:10.1016/j.ijmecsci.2019.105095

Marian, M., Almqvist, A., Rosenkranz, A., and Fillon, M. (2022). Numerical micro-texture optimization for lubricated contacts—A critical discussion. *Friction* 10 (11), 1772–1809. doi:10.1007/s40544-022-0609-6

Merkle, C. L., Feng, J., and Buelow, P. E. (1998). "Computational modeling of sheet cavitation," in *Proc. 3rd international symposium on cavitation, grenoble, France*.

Mikic, D., Desnica, E., Kiss, I., Mikic, V., et al.University Politehnica Timisoara, Faculty of Engineering Hunedoara, Romania (2021). Reliability analysis of rolling bearings considering the bearing radial clearance and operating temperature. *Adv. Eng. Lett.* 1 (No.1), 16–22. doi:10.46793/adeletters.2022.1.1.3

Morris, N., Leighton, M., La Cruz, M. de, Rahmani, R., Rahnejat, H., and Howell-Smith, S. (2015). Combined numerical and experimental investigation of the micro-hydrodynamics of chevron-based textured patterns influencing conjunctional friction of sliding contacts. *Proc. Institution Mech. Eng. Part J J. Eng. Tribol.* 229 (4), 316–335. doi:10.1177/1350650114559996

NGSolve (2025). Netgen/NGSolve finite element tool. Available online at: https://docu.ngsolve.org/latest/index.html.

Pusterhofer, M., Maier, M., Scharf, R., Haumer, F., and Grün, F. (2025). Hydrodynamic performance testing of artificial textures using a novel pin-on-disc test method. *Front. Mech. Eng.* 11, 1473028. doi:10.3389/fmech.2025.1473028

Ren, N., Nanbu, T., Yasuda, Y., Zhu, D., and Wang, Q. (2007). Micro textures in concentrated-conformal-contact lubrication: effect of distribution patterns. *Tribol. Lett.* 28 (3), 275–285. doi:10.1007/s11249-007-9271-4

Radojkovic, M., Stojanovic, B., Milojevic, S., Maric, D., Savic, S., Skulic, A., et al. (2023). Square openings as sources of stress concentration in parts of machines and devices. *Teh. vjesnik* 30 (2), 474–480. doi:10.17559/TV-20220603080026

Rahmani, R., Shirvani, A., and Shirvani, H. (2009). Analytical analysis and optimisation of the rayleigh step slider bearing. *Tribol. Int.* 42 (5), 666–674. doi:10.1016/j.triboint.2008.09.002

Rosenkranz, A., Costa, H. L., Profito, F., Gachot, C., Medina, S., and Dini, D. (2019). Influence of surface texturing on hydrodynamic friction in plane converging bearings - an experimental and numerical approach. *Tribol. Int.* 134, 190–204. doi:10.1016/j.triboint.2019.01.042

Savio, A., Cianferra, M., and Armenio, V. (2021). Analysis of performance of cavitation models with analytically calculated coefficients. *Energies* 14 (19), 6425. doi:10.3390/en14196425

Scharf, R., Maier, M., Pusterhofer, M., and Grün, F. (2024a). A comprehensive numerical study of a wedge-shaped textured convergent oil film gap. *Lubricants* 12 (4), 121. doi:10.3390/lubricants12040121

Scharf, R., Pusterhofer, M., Gussmagg, J., and Grün, F. (2024b). An investigation into the optimal dimple geometry in a single-dimple sliding contact. *Machines* 12 (9), 622. doi:10.3390/machines12090622

Scharf, R., Pusterhofer, M., and Grün, F. (2025). Numerical performance evaluation of single-dimple and multi-dimple textures under varying operating conditions - under review. *J. Tribol.*

Sharma, S., Jamwal, G., and Awasthi, R. K. (2019). Numerical study on steady state performance enhancement of partial textured hydrodynamic journal bearing. *Industrial Lubr. Tribol.* 71 (9), 1055–1063. doi:10.1108/ILT-03-2019-0083

Shen, Z., Wang, F., Chen, Z., Ruan, X., Zeng, H., Wang, J., et al. (2021). Numerical simulation of lubrication performance on chevron textured surface under hydrodynamic lubrication. *Tribol. Int.* 154 (3), 106704. doi:10.1016/j.triboint.2020.106704

Shibata, Y., and Enomoto, Y. (2018). "Global existence of classical solutions and optimal decay rate for compressible flows *via* the theory of semigroups," in *Handbook of mathematical analysis in mechanics of viscous fluids*. Editors Y. Giga and A. Novotný (Cham: Springer International Publishing), 2085–2181. doi:10.1007/978-3-319-13344-7_52

Singh, N., and Awasthi, R. K. (2021). Influence of texture geometries on the performance parameters of hydrodynamic journal bearing. *Proc. Institution Mech. Eng. Part J J. Eng. Tribol.* 235 (10), 2056–2072. doi:10.1177/1350650120982691

Sommer, D., Hornung, S., Esen, C., and Hellmann, R. (2024). Surface roughness optimization of hybrid PBF-LB/M-built inconel 718 using *in situ* high-speed milling. *Int. J. Adv. Manuf. Technol.* 132 (3-4), 1741–1751. doi:10.1007/s00170-024-13382-5

Su, B., Zou, X., Wang, Z., and Huang, L. (2024). Numerical analysis of lubrication properties on a bio-inspired parabolic textured surface. *Meccanica* 59 (6), 987–1000. doi:10.1007/s11012-024-01838-7

Uddin, M. S., Ibatan, T., and Shankar, S. (2017). Influence of surface texture shape, geometry and orientation on hydrodynamic lubrication performance of plane-to-plane slider surfaces. *Lubr. Sci.* 29 (3), 153–181. doi:10.1002/ls.1362

Ullah, M. Z., Rizwan, M., Raza, A., Ahmed, A., and Abid, M. (2021). "Effect of dimple shape and depth on tribological performance of textured surface," in *2021 international bhurban conference on applied sciences and technologies (IBCAST)*, 719–725. doi:10.1109/IBCAST51254.2021.9393183

Vencl, A., Ivanovic, L., Stojanovic, B., Zadorzhnaya, E., Miladinovic, S., and Svoboda, P. (2019). Surface texturing for tribological applications: a review. *Proc. Eng. Sci.* 1 (1), 227–239. doi:10.24874/PES01.01.029

Walther, C. (1931). Ueber die Auswertung von Viskositätsangaben. *Erdoel Teer* 7, 382–384.

Wang, J., Yan, Z., Fang, X., Shen, Z., and Pan, X. (2020). Observation and experimental investigation on cavitation effect of friction pair surface texture. *Lubr. Sci.* 32 (8), 404–414. doi:10.1002/ls.1520

Wang, X., Kato, K., Adachi, K., and Aizawa, K. (2001). The effect of laser texturing of SiC surface on the critical load for the transition of water lubrication mode from hydrodynamic to mixed. *Tribol. Int.* 34 (10), 703–711. doi:10.1016/s0301-679x(01)00063-9

Wang, W., He, Y., Zhao, J., Mao, J., Hu, Y., and Luo, J. (2020). Optimization of groove texture profile to improve hydrodynamic lubrication performance: theory and experiments. *Friction* 8 (1), 83–94. doi:10.1007/s40544-018-0247-1

Wang, J., Wang, Q., Li, Y., Guo, M., and Li, P. (2021). Numerical and experimental study on the effect of surface texture with roughness orientation considered under a mixed lubrication state. *Industrial Lubr. Tribol.* 73 (10), 1333–1341. doi:10.1108/ILT-06-2021-0204

Wang, Y., Jacobs, G., Zhang, S., Klinghart, B., and König, F. (2025). Lubrication mechanism analysis of textures in journal bearings using CFD simulations. *Industrial Lubr. Tribol.* 77 (1), 2–14. doi:10.1108/ILT-01-2024-0031

Wang, L., Zhang, C., Wei, W., Deng, T., Ma, T., and Shuai, P. (2025). Slope stability assessment using an Optuna-TPE-Optimized CatBoost model. *Eng* 6 (8), 185. doi:10.3390/eng6080185

Watanabe, S. (2025). DQM-POLYTECH-2023_S.Joksicatal_ResearchGate//tree-structured parzen estimator: understanding its algorithm components and their roles for better empirical performance. doi:10.48550/arXiv.2304.11127

Wei, Y., Tomkowski, R., and Archenti, A. (2020). Numerical study of the influence of geometric features of dimple texture on hydrodynamic pressure generation. *Metals* 10 (3), 361. doi:10.3390/met10030361

Xing, Y., Li, X., Hu, R., Long, X., Wu, Z., and Liu, L. (2021). Numerical analyses of rectangular micro-textures in hydrodynamic lubrication regime for sliding contacts. *Meccanica* 56 (2), 365–382. doi:10.1007/s11012-020-01296-x

Yang, J., and Palazzolo, A. (2021). Power loss reduction for tilt pad journal bearings utilizing pad pockets and steps. *Tribol. Int.* 159, 106993. doi:10.1016/j.triboint.2021.106993

Yu, H., Wang, X., and Zhou, F. (2010). Geometric shape effects of surface texture on the generation of hydrodynamic pressure between conformal contacting surfaces. *Tribol. Lett.* 37 (2), 123–130. doi:10.1007/s11249-009-9497-4

Zhang, Y. L., Zhang, X. G., and Matsoukas, G. (2015). Numerical study of surface texturing for improving tribological properties of ultra-high molecular weight polyethylene. *Biosurface Biotribology* 1 (4), 270–277. doi:10.1016/j.bsbt.2015.11.003